Journal of Structural Geology 32 (2010) 580–594

Contents lists available at ScienceDirect

Journal of Structural Geology

journal homepage: www.elsevier.com/locate/jsg

Deformation and recrystallization mechanisms in actively extruding salt fountain: Microstructural evidence for a switch in deformation mechanisms with increased availability of meteoric water and decreased grain size (Qum Kuh, central Iran)

Guillaume Desbois [a,*], Prokop Závada [b], Zsolt Schléder [c], Janos L. Urai [a]

[a] Structural geology, Tectonics and Geomechanics, RWTH Aachen University, Lochnerstr. 4-20, D-52056 Aachen, Germany
[b] Institute of Geophysics ASCR, v.v.i.; Boční II/1401, 141 31, Prague, Czech Republic
[c] Midland Valley Exploration Ltd., 144 West George Street, Glasgow, UK

ARTICLE INFO

Article history:
Received 6 July 2009
Received in revised form
10 March 2010
Accepted 11 March 2010
Available online 17 March 2010

Keywords:
Rocksalt
Salt extrusion
Gamma-irradiation
Deformation mechanisms
Microstructure

ABSTRACT

Microstructural study of rocksalt samples from an active salt fountain (Qum Kuh, central Iran) enabled to identify the relative contribution of different deformation mechanisms on extrusive salt flow. The microstructural study combined reflected and transmitted light microscopy of gamma-irradiated thin sections, textural analysis of digitized microstructures and Electron Back Scattered Diffraction (EBSD). Deformation microstructures record the strongly variable deformation conditions of salt flow in the diapiric system from the diapiric stem towards the distal part of the mature viscous fountain. High-stress deformation conditions typical for diapiric stems are recorded in the small subgrains within the porphyroclasts of all documented samples. Recovery and recrystallization due to divergent and decelerating flow associated with differential stress drop in the salt extrusion above the diapiric orifice is reflected by abundant growth band microstructures. This study reveals also evidence for penetration of rainwater into the salt mass and documents the switch from the dominant dislocation creep into dominant solution-precipitation creep from the upper part to the distal part of the fountain. This deformation mechanism switch is provided by influx of meteoric water and grain size decrease likely controlled by subgrain rotation and grain-boundary migration recrystallization.

1. Introduction

The properties of rocksalt are extensively discussed in the literature. Its multiple role in sedimentary basin evolution (Littke et al., 2008; McClay et al., 2003; Rowan et al., 1999), fluid sealing capacity for gas storage (Li et al., 2005), drilling problems in petroleum industry (Muecke, 1994; Wilson et al., 2002), the possibility of waste disposal in salt (Salters and Verhoef, 1980) and salt mining give the topic enormous economic importance and emphasize the need for the proper knowledge of the mechanical and transport properties of halite rocks deforming in nature (Drury and Urai, 1990; Urai and Spiers, 2007; Schoenherr et al., 2007a,b, 2009; Urai et al., 2008).

Zagros mountains (SE part of Iran) are the world-class site for well exposed salt extrusions and glaciers with up to 60 salt extrusions ranging in age from Cambrian to Pliocene displaying at least 6 different morphologies (Talbot, 1998; Jahani et al., 2007). Rocksalt extruding on flat topography through release-bends of major strike-slip faults in Zagros (Talbot and Alavi, 1996; Talbot and Aftabi, 2004) typically forms viscous fountains. However, most rocksalt in Zagros Mountains forms salt glaciers (namakiers) flowing down from the crests of the Zagros anticlines or through one or more fault gullies or uptilted river valleys (Talbot, 1998).

Salt glaciers were also extruded from diapirs in the Central European Basin during Triassic (Mohr et al., 2007). Vertical extrusion rates of salt extrusions (<10 mm/a) were recently measured using InSAR technique (Interferometric Synthetic Aperture Radar) (Weinberger et al., 2006; Hudec and Jackson, 2007; Aftabi et al., 2010) and also estimated by palinspastic reconstruction (Davidson et al., 1996; Bruthans et al., 2006). Active salt extrusions offer a unique opportunity to reconstruct deformation conditions for rocksalt based on identification of deformation mechanisms and constitutive equations from laboratory calibrations, experiments and theory. Because the measured flow laws are based on short-term laboratory tests and performed at high differential stresses, their precision is limited when extrapolated to low stress, long-term natural conditions. One key test for correct extrapolation of mechanical behavior of rocksalt is the direct comparison of the

* Corresponding author. Tel.: +49 241 80 95780; fax: +49 241 80 92358.
E-mail address: g.desbois@ged.rwth-aachen.de (G. Desbois).

0191-8141/$ – see front matter © 2010 Elsevier Ltd. All rights reserved.
doi:10.1016/j.jsg.2010.03.005

deformation mechanisms operative in nature and experiment (Passchier and Trouw, 2005).

Gamma-irradiation decoration is the most powerful technique for microstructural investigation of halite (Urai et al., 1987; Garcia Celma and Donker, 1996; Schléder and Urai, 2007; Schoenherr et al., 2009). The physical basis of the blue decoration of halite microstructures is the production of F-center defects by gamma-irradiation, which aggregate into sodium colloids (Van Opbroek and den Hartog, 1985). Because the colloids nucleate preferentially at solid-solution impurities and crystal-defect sites (Jain–Lidiard model), the resulting coloration reflects the halite microstructures. The intensity of the coloration is a function of the solid-solution impurities and crystal-defect density. Decoration of grain and subgrain boundaries is achieved by chemical etching of the thin sections (Urai et al., 1987). Combination of both kinds of decoration provides a rich detail of microstructure (subgrain-rich grain, strain free/new grains, growth bands, syn-sedimentary chevrons, grain-boundary indentation/truncation, edgewise propagation of subgrains, dissolution-precipitation features, core-mantle structure, pressure fringes) and used to infer qualitatively the deformation, recrystallization and fluid-transport mechanisms in studied samples (Urai et al., 1986a,b, 1987, 2008; Schléder and Urai, 2007; Schoenherr et al., 2009). Deformation mechanisms are also conveniently identified using EBSD for CPO measurements (Schléder and Urai, 2007) together with grain size and shape statistics, while subgrain size statistics is used for piezometric estimates of differential stress (Schléder and Urai, 2005).

While solution-precipitation accommodated grain-boundary sliding (GBS) is typically associated with low degree of CPO and abundant substructure-free equant grains (Schléder and Urai, 2007), dynamic recrystallization by dislocation creep is typical with large variety of substructure richness in the grains and well-developed CPO (Passchier and Trouw, 2005). The grain size of samples is controlled by two competing deformation mechanisms during dynamic recrystallization: subgrain rotation (SGR) and grain-boundary migration (GBM) recrystallization. SGR tends to decrease the average grain size of the aggregates and is typical with low-angle misorientation of marginal subgrains from cores of porphyroclasts and its dominant activity is manifested by similar size of subgrains and adjacent new grains in the matrix (Halfpenny et al., 2004). In contrast, GBM generally increases grain size of the dynamically recrystallizing aggregate. GBM recrystallization in combination with SGR can also result in grain size decrease, but regardless to the size of subgrains developed in porphyroclasts (Passchier and Trouw, 2005).

Previous studies (Talbot and Rogers, 1980; Urai et al., 1986b; Schléder and Urai, 2007; Urai and Spiers, 2007; Schoenherr et al., 2009) suggest that dislocation-creep-accommodated dynamic recrystallization and pressure-solution creep both govern rheology of active salt extrusions. Various creep laws are available (e.g. Carter et al., 1993 and Spiers et al., 1990) to describe the specific deformation mechanisms. However, the salt flow is best described by a multi-mechanism creep equation and deformation map for rocksalt, which combine the flow laws for different deformation mechanisms (Spiers and Carter, 1998) and suggest that under natural conditions flow will occur either by climb-controlled dislocation creep and/or pressure-solution depending on the grain size (Schléder, 2006; Urai et al., 1986b, 2008). Activity of these deformation mechanisms is also strongly promoted by inter-granular fluid (Urai and Spiers, 2007), that was incorporated in the salt mass during its deposition (Schléder and Urai, 2005) or by influx of meteoric water into extrusive salt, which together with small grain size provide suitable conditions for dominant solution-precipitation creep and accelerate salt flow in the salt glaciers (Jackson, 1985; Urai, 1987). In contrast, for relatively large grain size of domal salts (2–20 mm), dislocation-creep-accommodated dynamic recrystallization is dominant.

Schléder and Urai (2007) suggested that the salt flow in the extrusion of Tertiary rocksalt in the Eyvanekey plateau was heterogeneous and was accommodated primarily by several mylonitic shear zones, where salt deformed exclusively by solution-precipitation creep and grain-boundary sliding (GBS) at grain size of 0.6 mm, while in protomylonites between the shear zones with grain size of 2–6 mm, salt deformed by combination of dislocation and solution-precipitation creep with GBS. Schoenherr et al. (2009) reported that the rocks salt microstructure of surface-piercing diapirs of Ara Salt in Oman records an overprint of dislocation creep microstructures originated in the diapiric stem by recrystallization and solution-precipitation creep producing static growth of new grains and fibrous microstructures. This salt also contains elongated pores parallel with long axes of grains, which we interpret as zones of salt leaching by meteoric water (see Fig. 8 in Schoenherr et al., 2009).

This paper presents a detailed microstructural study of salt samples collected from the active Qum Kuh salt fountain in Central Iran (Talbot and Aftabi, 2004; Schléder, 2006). Our goal is to distinguish specific deformation mechanisms active at different topographic positions of a mature and active salt extrusion (top, middle and distal parts of the fountain respectively) in order to understand their relative contribution to the flow of rocksalt and to identify what processes control the anticipated switch of deformation mechanisms in extrusive salt systems (Urai et al., 1986b). Our study is based on microstructural analysis of blue thin sections from rocksalt decorated by gamma-irradiation, quantitative analysis of the microstructures and CPO (crystal preferred orientation) measurements using EBSD.

2. Local geology and sampling sites

Several diapirs of the Lower Oligocene Lower Red Fm and Lower Miocene Upper Red Fm salt sequence reach the surface in central Iran forming salt glaciers or salt fountains (Fig. 1; Jackson et al., 1990). Those include the Qum Kuh fountain near the city of Qum, some 150 km SSW of Tehran (Gansser, 1960; Jackson et al., 1990; Talbot and Aftabi, 2004). The salt emerged from a depth of 5 to 3 km along a releasing bend in a major dextral transpressive fault crossing the Qum basin (Jackson et al., 1990; Talbot and Aftabi, 2004). Talbot and Aftabi (2004) suggested that the salt surface flows at a rate of 82 mm/a through a 1.5 × 1 km vent and that the extrusion lasted at least 42 000 years. In contrast, satellite interferometry data reveal uplift of about 10 mm/a (see Fig. 29 in Hudec and Jackson, 2007). The salt hill is 3 km wide and rises 315 m above the surrounding plateau. From the vent, the salt fountain spreads ~0.75 km to the west and ~2 km to the south (Fig. 1; Gansser, 1960; Talbot and Aftabi, 2004). The complex surface pattern of the salt layering reflects multiple repetition of the initial salt stratigraphy by folds and several deformation phases (Fig. 1; Talbot and Aftabi, 2004). The rocksalt throughout the fountain belongs to the multicolored Upper Red Formation of Lower Miocene age and consists of halite with minor buff anhydrite and trace of red clay and green volcanic ashes. White salt of Lower Red Formation (Lower Oligocene) occurs locally at the base of the allochthonous salt (Talbot and Aftabi, 2004).

In a field campaign, we collected 20 samples from different locations in the salt fountain. For this study, we selected seven samples (Fig. 1.b) including two samples (1.1 and 1.3) from the top of the fountain, two samples (2.5 and 2.6) from the southern hillside (middle part of the fountain) and three samples (1.7, 1.4 and 9.3) collected in a quarry located on the western margin of the fountain (distal part, Fig. 1.d). Samples from the top and middle

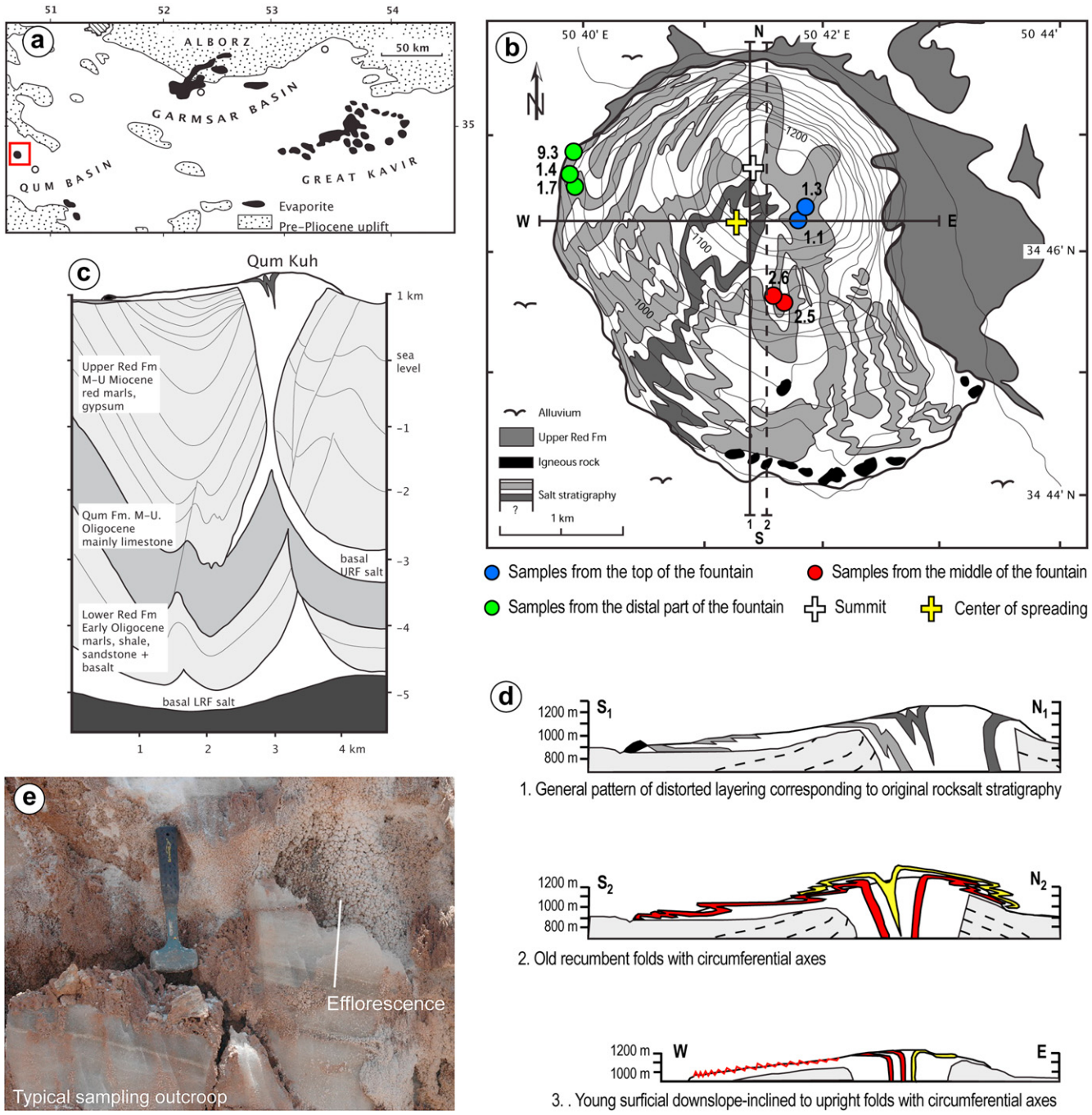

Fig. 1. Simplified regional setting of Qum Kuh rocksalt fountain (central Iran): (a) Surfaced evaporites in the Garmsar basin and adjoining Qum and Great Kavir basins (after Jackson et al., 1990). The location of the study area is indicated with a rectangle; (b) Simplified map of the Qum Kuh with sampling localities, topographic contours and stratigraphy indication (c) Cross-section throughout the salt structure of Qum Kuh, no vertical exaggeration; (d) Cross-sections of fountain structures from profiles indicated in (b): 1) General pattern of distorted layering corresponding to original rocksalt stratigraphy along south–north profile; 2) and 3) show simplified profiles depicting old and new recumbent flow folds with circumferential axes omitting local complications due to radial folds. (e) Typical sampling outcrop showing efflorescence pattern (hammer for scale). (b), (c) and (e) are re-drawn from Talbot and Aftabi (2004).

parts of the fountain represent the Upper Red Formation salt, whereas three samples from the distal part represent the white salt of Lower Red Formation (Fig. 2).

3. Sample preparation and methods

Raw samples were first cut into slabs (6 × 6 × 2 cm) with small amount of water to prevent micro-cracking. The slabs were gamma-irradiated in the Research Reactor of Jülich (Germany) at 100 °C with dose rate of 3–4 kGy/h to a total dose of 5.7 MGy. Etched thin sections were prepared parallel to the lineation and perpendicular to the foliation following the technique described by Schléder and Urai (2005). The microstructure was inspected in transmitted and reflected light microscope. EBSD mapping of CPO was performed on a scanning electron microscope CamScan3200 (Czech Geological Survey, Prague) and LEO1530 Gemini FESEM (University of Bochum, Germany), both equipped with a Nordlys EBSD detector. Pattern acquisition was carried out using

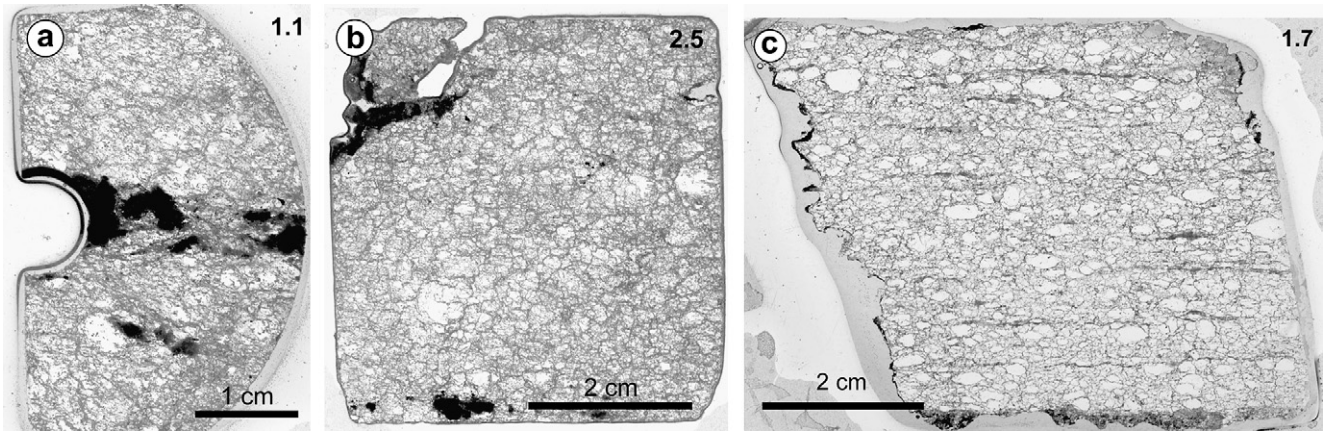

Fig. 2. Scanned thin sections of selected samples. Dark patches are second phases, mostly buff anhydrite, in the rocksalt. (a) Sample 1.1 is from the top part of the fountain; (b) sample 2.5 from the middle part of the fountain, and (c) sample 1.7, is from the distal part of the fountain.

acceleration voltage of 20 kV, beam current of 5–8 nA and 33 mm working distance, using step size of 10 and 20 μm. The EBSD patterns were indexed with the HKL Channel 5 software. The quality of EBSD patterns was very high; therefore more than 90% of measured points were successfully indexed. The maps were further processed to remove erroneous data and to provide more complete reconstruction of the microstructure (Prior et al., 2002; Bestmann and Prior, 2003). Axial ratio of grains, together with eigenvalue ratios of their matrix of inertia (shape preferred orientation) and grain and subgrain sizes were statistically evaluated using the PolyLX Matlab toolbox (Lexa et al., 2005; http://petrol.natur.cuni.cz/~ondro/polylx:home) from microstructures digitized in ArcView 3.2 from micrographs.

4. Results

4.1. Microstructural observations

4.1.1. Samples from the top of the salt fountain

Samples from the vicinity of salt fountain summit show fabric made of 0.5–1 mm large equigranular sub-euhedral grains with minor porphyroclasts (>1 mm in size) (Fig. 3, samples 1.1 and 1.3). The porphyroclasts have subgrain-rich cores and interlobated grain boundaries. Subgrains are homogeneous in size and slightly elongated (Fig. 3.c). Subgrain-rich cores exhibit blue patches surrounded by white halo (Fig. 3.b), which resemble but do not completely match the subgrain boundaries as revealed by the etching technique (Fig. 3.c). Small grains (less than 500 μm in size) are euhedral and subgrain-free (Fig. 3.b). The euhedral grains are decorated with deep blue bands that are parallel to their outer edges. The bands are more clearly developed in grains that are adjacent to the large subgrain-rich grains. Truncation relationships are typical for interfaces between two banded grains (Fig. 3.e). Grains in the size range of 0.5–1 mm (Fig. 3.d) are sub-euhedral and have a subgrain-rich core surrounded by more intense blue and banded, but subgrain-poor rim. In the rim, white-decorated subgrain boundaries crosscut the deep blue bands (Fig. 3.d). Grain boundaries between the porphyroclasts and the smaller subgrain-poor grains contain arrays of fluid inclusions, while the grain boundaries between the small grains are fluid-inclusion-free.

4.1.2. Samples from the middle part of the fountain

Salt collected from the middle part of the fountain reveals similar microstructure and grain size (see Table 1, Fig. 4, samples 2.5 and 2.6) as that from the top of the fountain: 0.5–1 mm large, subgrain-free sub-euhedral grains and few subgrain-rich interlobated porphyroclasts (>1 mm in size, Fig. 4.a). Dark blue and subgrain-free grains have either rectangular edges on the contacts with subgrain-rich grains (Fig. 4.b,c) or truncated contact (Fig. 4.e), where two subgrain-free grains are adjacent. Grains (about 500–700 μm in size) with subgrain-rich core and subgrain-free mantles are also present. The subgrain-free rim is locally crosscut by white-decorated subgrain boundaries directing from the grain core towards the margin (Figs. 4.d and 5.c). Distribution of fluids at grain boundaries is similar to that observed in the samples from the top of the fountain.

In one thin section, the salt is affected by several inter- and intra-granular cracks that dip at shallow angles towards the front of the fountain (sample 2.6, Fig. 5). Pores with smooth boundaries elongated parallel with the sub-horizontal system of anisotropy-related joints (Talbot and Aftabi, 2004) occur within or between the grains. The pores have up to 0.5 cm in their long dimension. The cracks are partially sealed and predate salt precipitates of dark blue color (Fig. 5.b,c). Dark blue salt decorating most of the inter-granular boundaries and the intra-granular cracks defines a pervasive and partly sealed crack network that penetrates the entire volume of the studied specimen (Fig. 5.a). At higher magnification, the inter-granular deep blue salt filling from this network is characterized by irregular wavy banded structures (Fig. 5.d) made of discontinuous white fluid-inclusion-rich bands alternating with blue fluid-inclusion-poor bands (Fig. 5.e).

4.1.3. Samples from the distal part of the fountain

In the three thin sections from the distal part of the fountain, the grain size distribution is bimodal approximately 2 mm-size porphyroclasts surrounded by small, <1 mm sub-euhedral grains (Fig. 6). Each thin section exhibits different proportion of porphyroclasts and small sub-euhedral grains (Fig. 6). Sample 1.4 shows abundant porphyroclasts with homogeneous blue subgrain-free cores surrounded by a white mantle about 200–500 μm thick containing numerous subgrains less than 150 μm in size (Fig. 6.a). The small sub-euhedral grains (<1 mm) are patchy-blue with only few well-developed subgrains. Sample 9.3 (Fig. 6.b) reveals subgrain-rich porphyroclasts with blue patchy core and white tails containing white or pale blue subgrains (about 100 μm long), which are mostly elongated parallel to the stretching lineation (Fig. 7.e). Finally, in sample 1.7 (Fig. 6.c), porphyroclasts are deep-blue decorated, subgrain-rich and rarely exhibit the white subgrain-rich rims observed for the porphyroclasts as in sample 1.4 (Fig. 6.a). The surrounding sub-euhedral grains are homogeneously blue and subgrain-free (Fig. 7.c,d). Where growth bands are visible, they are clearly truncated by neighboring grains (Fig. 7.f). Fluid inclusion distribution at grain boundaries is similar to that observed in samples from the top and middle parts of the

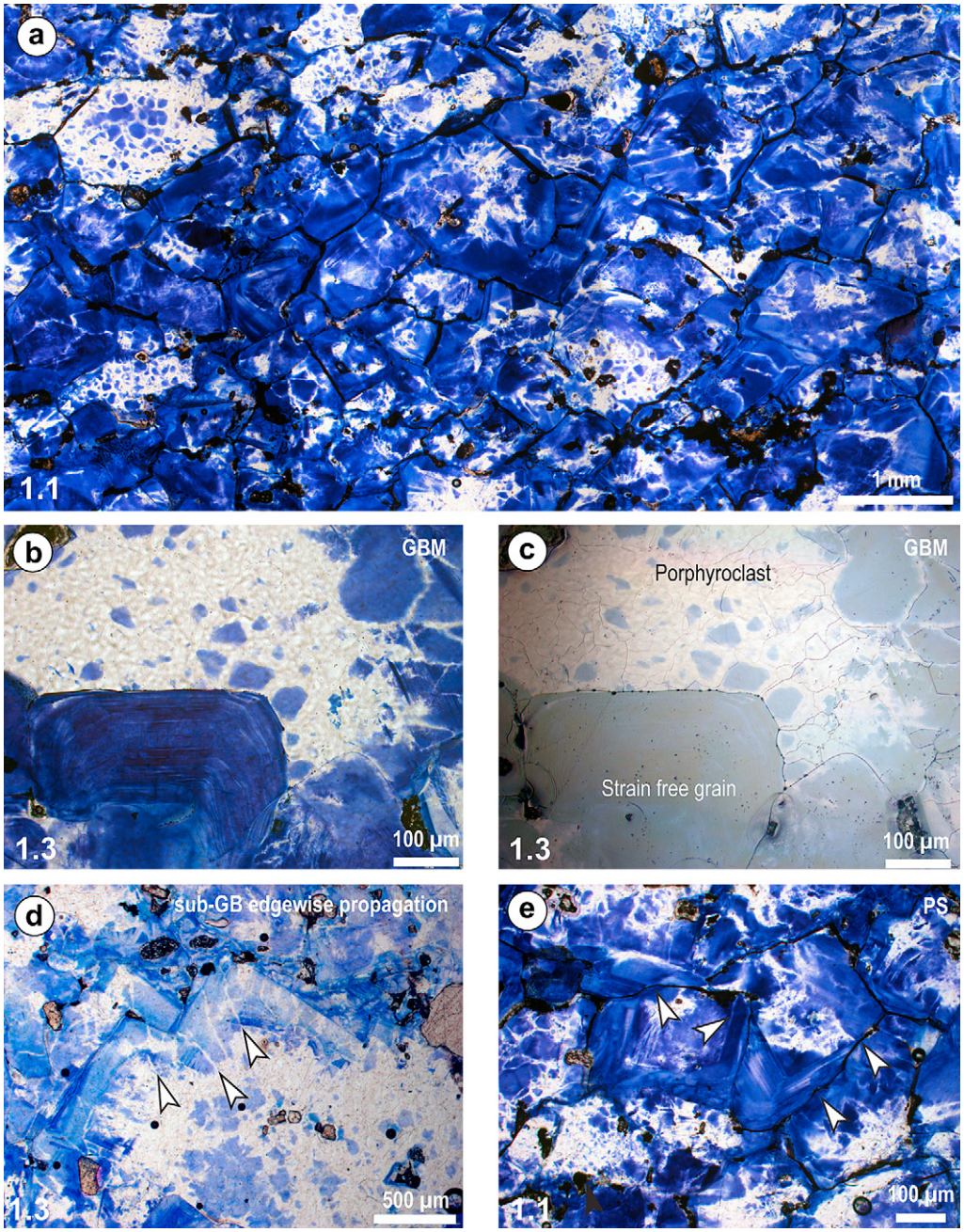

Fig. 3. Transmitted light and reflected light micrographs typical for samples collected at the top of the fountain. (a) Overview of the fabric at low magnification showing equigranular sub-euhedral grains (0.5–1 mm large) and some minor larger porphyroclasts (>1 mm in size). (b) Substructure-free grain rimmed by growth bands embayed by a subgrain-rich grain in transmitted light point to GBM, (c) reflected light micrograph of area (b). Note that, the cellular blue pattern revealed by gamma-irradiation does not match exactly the subgrain boundary network revealed by the etching technique. (d) Subgrain-rich core with new subgrain-poor rim exhibiting growth bands. The new subgrain-poor rim is crosscut by several white lines (indicated by white arrows) reflecting the edgewise propagation of highly misoriented subgrain boundaries behind the migrating grain boundary. (e) Truncation of growth bands (the direction of indentation is indicated by white arrow) pointing to zone of preferential PS. On each micrograph, the stretching lineation is horizontal. Sample number is indicated in the lower left corner of each micrograph.

fountain (Fig. 8). Samples 9.3 and 1.7 reveal similar microstructures as the mylonites described by Schléder and Urai (2007) from the Garmsar hills and Eyvanekey plateau.

4.2. Quantification of textures

4.2.1. Quantitative analysis of microstructures

Quantitative microstructures for all thin sections from salt fountain (Table 1) include mean grain and subgrain size, axial ratio and calculated differential stress using the piezometric equation D (µm) = 215 $\sigma^{-1.15}$ (MPa) (Schléder and Urai, 2005; Urai and Spiers, 2007). To describe grain and subgrain sizes, we used the geometric mean and the difference between the third and first quartile (grain-size spread), which are the most representative values characterizing the log-normal distribution (Lexa et al., 2005). Grain sizes of samples collected in the upper and middle part of the fountain (samples 1.1, 1.3, 2.5 and 2.6) range between 400 and 600 µm in diameter whereas grain size of samples from the distal part of the fountain is relatively smaller, 210–330 µm (samples 1.7 and 9.3). The grain size spread also generally decreases from the top-middle part

Table 1
Quantitative analysis of microstructures performed on grains and subgrains.

Samples	Grains					Sub-grains			
	N	Grain size		Axial ratio		*N*	Sub-grain size		Differential stress (MPa)
		Geomean (mm)	Q_3-Q_1	Geomean	Q_3-Q_1		Geomean (mm)	Q_3-Q_1	
Top									
1.1	147	0.442	0.425	1.441	0.360	717	0.038	0.029	4.5
1.3	57	0.413	0.312	1.491	0.446	–	–	–	–
Middle									
2.5	205	0.423	0.303	1.422	0.466	388	0.049	0.034	3.6
2.6	96	0.594	0.461	1.413	0.397	591	0.058	0.045	3.1
Front									
1.4	279	0.391	0.385	1.648	0.596	850	0.047	0.036	3.8
1.7	628	0.214	0.181	1.562	0.506	1164	0.036	0.025	4.8
9.3	234	0.327	0.291	1.606	0.515	1619	0.038	0.032	4.5

N: number of objects analyzed (grain or subgrains).
Q_3-Q_1: difference between the third and first quartile; i.e., grain size spread.
Geomean: Geometric mean – most representative value for log-normal distribution.
The differential stress is calculated by sub-grain size piezometry using the equation from Schléder and Urai (2005).

(Q_3-Q_1 = 0.3–0.5) to the distal part of the fountain (Q_3-Q_1 = 0.18–0.3), except for sample 1.4, where both grain size and grain size spread are similar to the samples from the top and middle part of the fountain. In contrast, the axial ratio of grains increases from values around 1.46 at the top to 1.6 in distal part of the fountain. Subgrains from subgrain-rich porphyroclasts measured in all investigated samples reveal size between 36 and 58 μm corresponding to differential stresses in the range of 3.1–4.8 MPa.

4.2.2. EBSD measurement on samples from the distal part of the fountain

An EBSD map depicting the crystallographic orientation of 726 grains measured within 8 × 3 mm area of sample 1.7 is presented in Fig. 9. The CPO (crystallographic preferred orientation) pattern is close to random. Only few low degree misorientation boundaries in the map of crystallographic orientation (Fig. 9.b) confirm the microscopic observation that the small grains have no substructure. Subgrains are indicated in some of the larger grains by domains of low misorientation with respect to the host grain. For sample 9.3, EBSD mapping was performed in three distinct areas in the neighborhood of substructure-rich porphyroclasts surrounded by subgrain-poor grains to test, whether the new grains form by progressive subgrain rotation of subgrains in the rims of porphyroclasts. The maps revealed porphyroclasts containing subgrains with dominant misorientations from 2 to 5° with a few boundaries between 5 and 10° and very rarely with 10–15° (a representative EBSD map is shown in Fig. 10). Misorientation of 15° was taken as lower limit for high-angle grain boundary (Bestmann et al., 2005). Comparing the etched thin section images and the EBSD patterns (Fig. 10.a,b), it is apparent that some of the subgrain boundaries do not occur on the EBSD map, indicating that these boundaries have a lower misorientation degree than 2° (Trimby et al., 2000). The misorientation profiles indicated in Fig. 10.b reveal that the misorientation degree increases from the porphyroclast core towards the new adjacent grain (Profile A-B, Fig. 10.d). The misorientation change is gradual within the porphyroclasts. Similarly, profile C-D (Fig. 10.d), reveals a step-like and increasing then decreasing degree of misorientation from one porphyroclast to another. This profile and the stereographic projection data (Fig. 10.c) show that the crystallographic orientation of both porphyroclasts is similar.

5. Discussion

Microstructural analysis of the rocksalt samples collected on the active Qum Kuh salt fountain enabled identification of several deformation mechanisms that contribute to viscous salt flow. Their relative activity depends on the location within the extrusive salt fountain. We also found microstructural evidence for rainwater penetration into the fountain, which can cause weakening of salt by enhancement of fluid-assisted deformation mechanisms. Results are explained in the tectonic framework of this extrusive diapir.

5.1. Deformation and recrystallization mechanisms inferred from the selected samples

As suggested by microstructural observations, the flow of rocksalt in the fountain is provided by dynamic recrystallization, including both grain-boundary migration (GBM) and subgrain rotation (SGR) together with pressure-solution (PS) accommodated grain-boundary sliding (GBS). These mechanisms operate simultaneously in deforming salt throughout the salt fountain, although the evidence for relative dominance of PS-accommodated GBS increases from the top to the distal part at the expense of dynamic recrystallization.

5.1.1. Dynamic recrystallization

All gamma-irradiated samples investigated in this study show evidence for growth bands, which reflect changes in grain-boundary fluid chemistry or migration rate during grain-boundary migration (Schléder and Urai, 2005; Murata and Smith, 1946). Growth bands appear either in small subgrain-free grains in contact with subgrain-rich porphyroclasts (Figs. 3.b,c and 4.b,c) or in the subgrain-free rim of subgrain-rich core grains in contact with subgrain-rich porphyroclasts (Figs. 3.d,e and 4.b). The subgrain-poor grains with growth bands are interpreted to consume subgrain-rich grains by GBM (Guillopé and Poirier, 1980).

The subgrain-rich core in larger grains may be surrounded by banded rim with elongated subgrains (Figs. 3.d, 4.d and 5.c). These are interpreted to reflect the edgewise propagation of subgrains behind migrating grain boundaries (Means, 1983; Means and Ree, 1988; Ree, 1991). This process is similar to that found in bischofite (Urai, 1983, 1987) and octachloropropane (Means, 1983; see also Urai et al., 1986a), where the dominant process during dynamic recrystallization is simply the migration of pre-existing high-angle grain boundaries, without the formation of new grains sensu stricto (Urai et al., 1987).

Considering a large variety of “substructure richness” in the samples from the top and middle part of the fountain and abundant growth bands with edgewise propagated subgrains we interpret the growth bands as a result of strain-induced GBM rather than

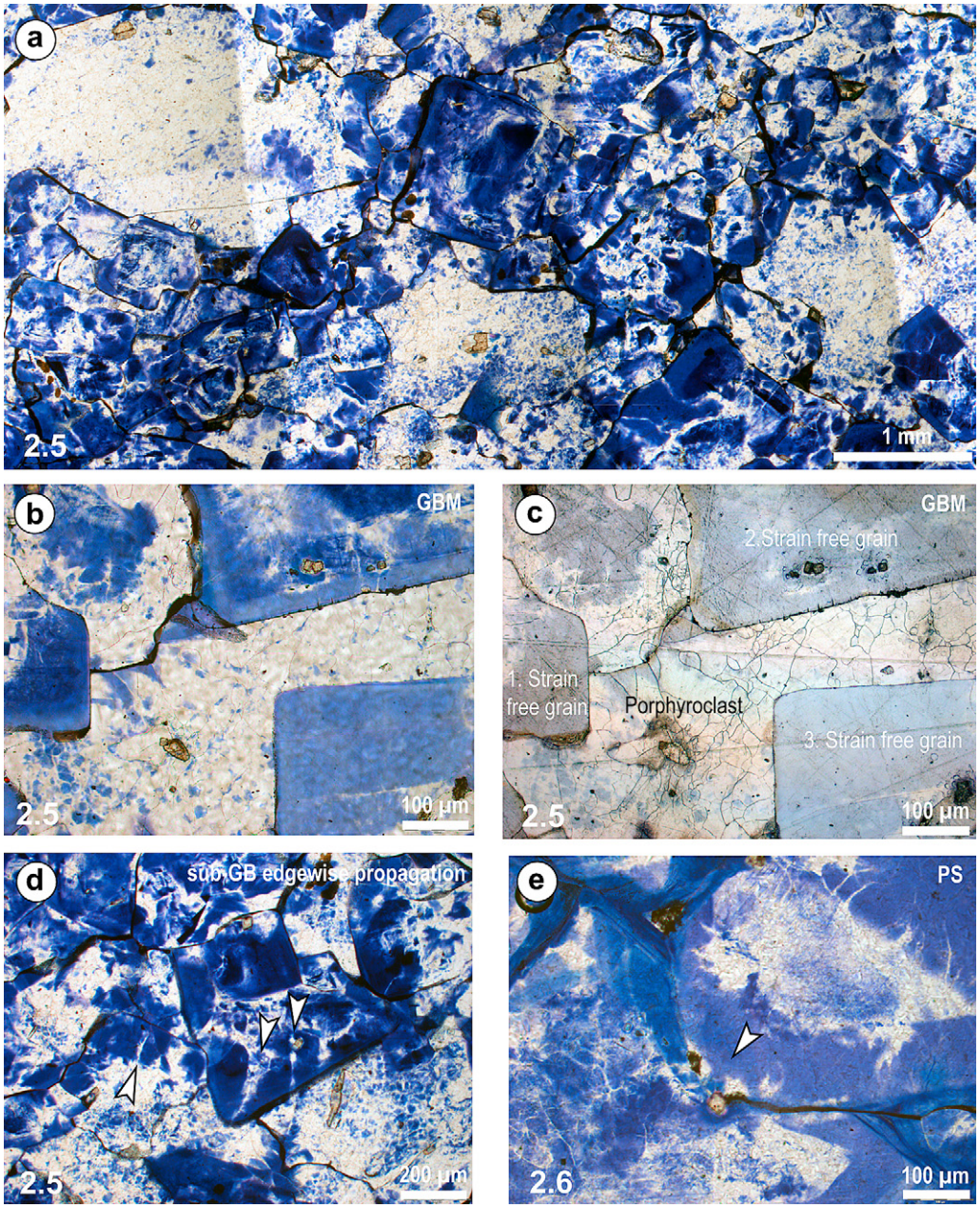

Fig. 4. Transmitted and reflected light thin section micrographs of gamma-irradiated samples collected in the middle part of the fountain. (a) Overview of the thin section at low magnification showing equigranular sub-euhedral grains (0.5–1 mm large) and some minor larger porphyroclasts (>1 mm in size). (b) Subgrain-rich old grain in contact with three new subgrain-free grains in transmitted light, (c) shows reflected light micrograph of area (b), (d) banded rims in mantle of grains reveal highly misoriented subgrain boundaries (white arrows). (e) Truncation of growth bands (the direction of indentation is indicated by white arrow). On each micrograph, the stretching lineation is horizontal. Sample number is in the lower left corner of each micrograph.

static annealing. The latter is typical for elevated temperatures (Piazolo et al., 2006) or high differential stress (Schenk and Urai, 2004) and can be excluded for conditions occurring in extrusive salt (<50 °C, <1 MPa in salt glacier; Schléder and Urai, 2007; and <5 MPa for the domal salt; this paper, Table 1). Although static recrystallization was suggested to be responsible for grain size growth for a very coarse-grained (up to 14 cm) Ara salt type on the top of surface-piercing diapir in Oman (Schoenherr et al., 2007a), that could be alternatively explained by passive transport of coarse-grained salt domain in undeformed state from greater depths as an inclusion within the surrounding finer-grained salt. Non-banded, substructure-free grains with sub-euhedral boundaries in the vicinity of porphyroclasts in the samples from the distal part of the fountain (Fig. 7.c,d) are also interpreted as a result of strain-induced GBM.

Porphyroclasts with subgrain-rich margins (Figs. 6.a and 7.a,b) observed in samples from the distal part of the fountain are typical for SGR (Stipp et al., 2002; Drury and Urai, 1990; Passchier and Trouw, 2005). Though such mechanism has not been clearly proved to be operative in halite in natural conditions. However, our EBSD results corroborate also SGR (Fig. 10), where marginal subgrains are progressively misoriented from the center towards the rim of porphyroclasts. Considering the significantly larger grain sizes of the substructure-poor grains in mantles of porphyroclasts than the subgrains (Fig. 7.c,d; Table 1), the new grains are interpreted as originated by combined activity of SGR and GBM.

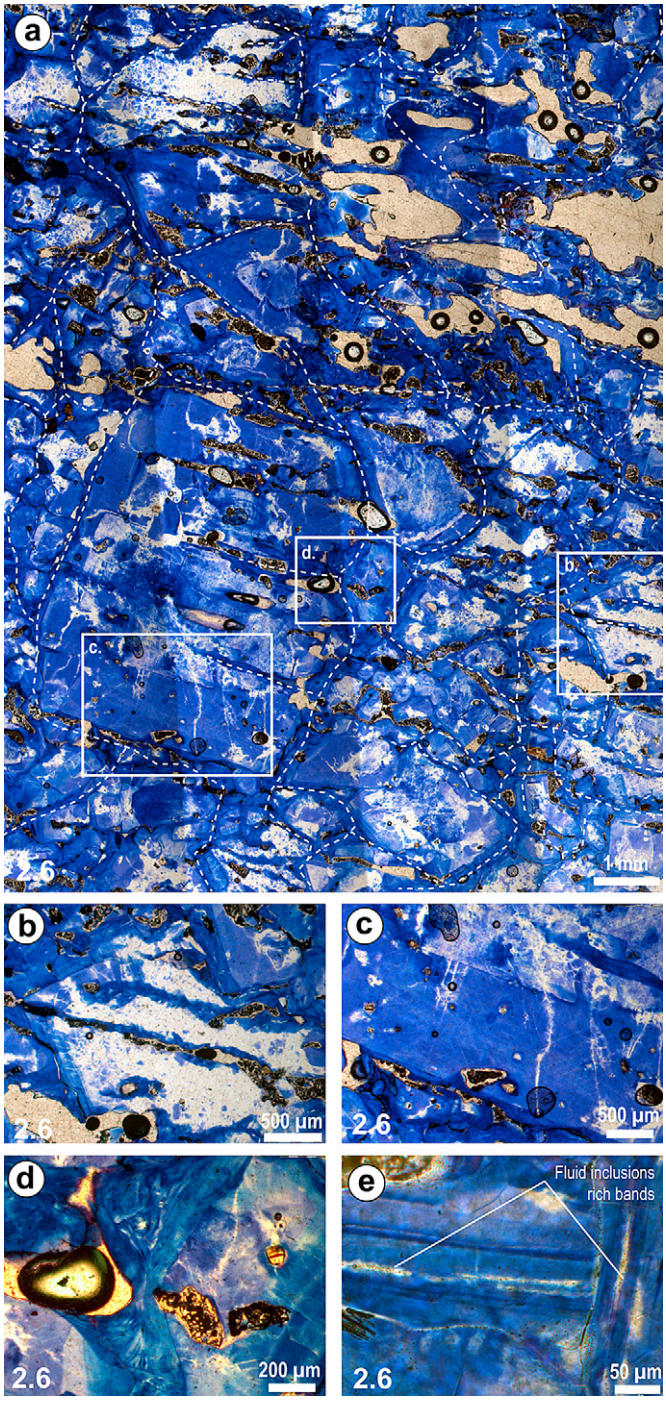

Fig. 5. Transmitted light thin section micrographs of gamma-irradiated sample collected in the middle part of the fountain. (a) Overview of the fabric at low magnification revealing large grains with subgrain-rich core and subgrain-poor rim and few smaller subgrain-poor grains. Numerous inter-granular sub-horizontal cracks segment the whole sample. The dashed white lines outline the pervasive inter- and intra-granular network of precipitated brine. At this scale, the brine is slightly deeper blue than the surrounding. (b) A large subgrain-rich core/new subgrain-poor rim grain segmented by cracks, which are partially sealed by late salt precipitates. (c) Focus area of the new subgrain-poor rim. The new subgrain-poor rim is crosscut by white line reflecting highly misoriented subgrains. (d) Focus on the deep blue salt precipitated in inter-granular channels showing irregular wavy banded structures. (e) Higher magnification of the wavy banded structures depicted in (d) reveals white irregular and discontinuous fluid-inclusion-rich bands alternating with blue fluid-inclusion-free bands. On each micrograph, the stretching lineation is horizontal. Largest pores with smooth grain boundaries are resulted from leaching of the rocksalt by rainwater (now filled with epoxy resin). Sample number is in the lower left corner of each micrograph.

The grain boundary between the subgrain-rich grains and subgrain-free grains invariably contains arrays of fluid inclusions. We assume that this fluid is the original fluid present on grain boundaries before sampling and that it was not introduced during etching of the thin sections. Trace amount of brine greatly increases the grain-boundary mobility and induces dynamic recrystallization by fluid-assisted grain-boundary migration (e.g. Watanabe and Peach, 2002).

5.1.2. Solution-precipitation

Truncation of growth band microstructures by neighboring grain boundaries (Figs. 3.e; 4.e and 7.f) pointing to dissolution during solution-precipitation creep are present in all studied samples. Similar microstructures originated by solution-precipitation creep were reported by Spiers et al. (1990) in porous polycrystalline halite containing saturated brine. The elongated subgrains in the tails of porphyroclasts from samples of the distal part of the fountain (Figs. 6.b and 7.e) are interpreted as overgrowths that typically form in the pressure shadows of rigid clasts and reflect pressure-solution creep together with grain-boundary sliding process (Schléder and Urai, 2007; Schoenherr et al., 2009). Inter-granular fluid identified on grain boundaries (Fig. 8) is essential for pressure-solution (Lehner, 1995; Schutjens and Spiers, 1999; Spiers et al., 2004; Passchier and Trouw, 2005). Though evidence for dislocation creep regime were also found in samples from the distal part of the fountain (Fig. 7.a-d, see section 5.1.3), the absence of CPO in sample 1.7 (Fig. 9) and the abundance of pressure fringes around rigid clasts only visible in other samples from the distal part of the fountain (samples 1.4, 9.3; Fig. 7.e) suggest that pressure-solution-accommodated GBS is the dominant deformation mechanism active in the distal part of the fountain, which is corroborated by the relatively smaller grain size (Spiers and Carter, 1998; Table 1).

5.2. Possible incorporation of rainwater into rocksalt microstructures

In the gamma-irradiated sample 2.6 (Fig. 5), which was collected at the surface of the middle part of the fountain, the boundaries and also sub-horizontal inter-granular fractures impregnated by dark blue salt characterize an interconnected network. The dark blue salt is interpreted as crystallized brine that penetrated into the porous salt mass after rainfall. Sub-horizontally elongated pores in the specimens also likely reflect parts leached by halite-unsaturated rainwater penetrating the surficial layer of the salt fountain. The micro-channels that streamlined the meteoric water are manifested by irregularly banded dark blue salt with discontinuous fluid-inclusion-rich bands, “hugger-mugger” wavy bands and lack of any grain and subgrain structures (Fig. 5.d,e). These are clearly different from straight fluid-inclusion-outlined arrays and chevrons characteristic primary (syn-sedimentary) structures (Schléder and Urai, 2005). The origin of porosity in salt is commonly micro-cracking and dilatancy at high fluid pressure or low mean stress (Urai et al., 2008; Schoenherr et al., 2007b). However, the long-term stress conditions at the surface of the extrusive salt do not meet these requirements for dilatancy. We propose that the porosity in the rocksalt on the surface of the salt fountain is promoted by joints that form due to diurnal and seasonal thermal contraction and expansion (Talbot and Aftabi, 2004), which can cause intra- and inter-granular micro-cracking. In addition, rainwater influx can also exploit dilational joint systems that occur parallel and perpendicular to the mechanical anisotropy provided by the compositional layering and/or the grain-shape fabric. These up to three orthogonal joint systems are present on almost every salt outcrop as described by Talbot and Aftabi (2004). The vertical joints affecting the surficial rocksalt should also slowly dilate as this surficial

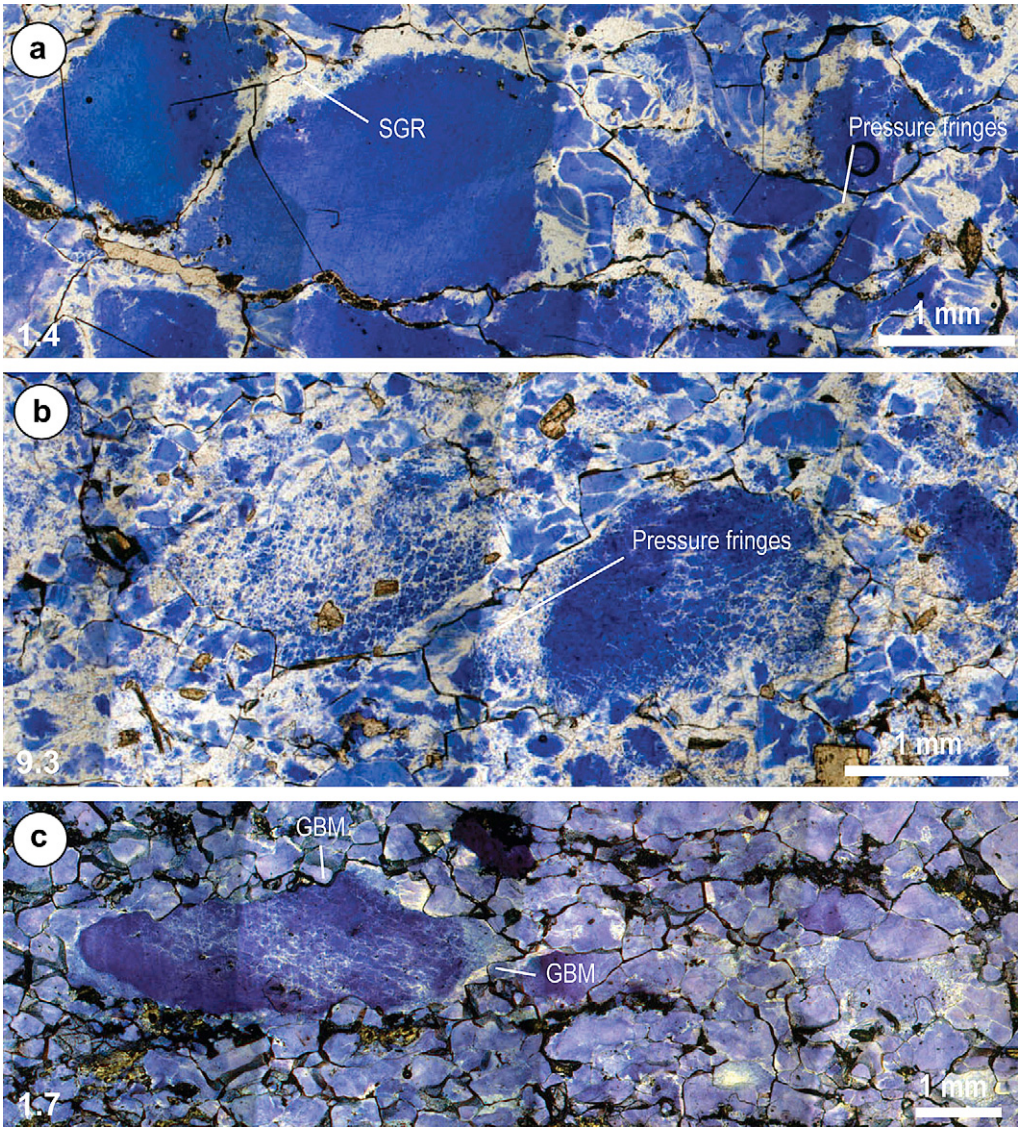

Fig. 6. Transmitted light thin section micrographs of gamma-irradiated samples from the distal part of the fountain, showing small (<1 mm) sub-euhedral grains surrounding the porphyroclasts (2 mm long in their longer dimension), (a) Sample 1.4; large porphyroclasts with deep blue subgrain-free cores surrounded by thin white subgrain-rich rim. (b) Sample 9.3; large and subgrain-rich porphyroclasts enclosed in subordinate fine-grained matrix of small polygonal grains. Pale blue or white elongated subgrains occur in pressure shadows around some porphyroclasts with deep blue color in the core. (c) Sample 1.7; porphyroclasts are deep blue with numerous subgrains developed in a narrow zone crosscutting obliquely the entire porphyroclast, porphyroclasts are surrounded by sub-euhedral grains, which are homogeneously blue and subgrain-free. On each micrograph, the stretching lineation is horizontal. Sample number is in the lower left corner of each micrograph.

carapace extends due to continuous growth/inflation of the viscous fountain. Identification of this micro-scale crack network marked by newly precipitated brine (Fig. 5.a) suggests that meteoric water can be incorporated into the salt rock microstructure as fluid inclusions trapped in the inter-granular network (Fig. 5.e) and can be later re-mobilized to enhance the rate of deformation mechanisms in rocksalt (Schenk and Urai, 2005; Schmatz and Urai, 2009). The sub-horizontal elongation of smooth shaped pores suggests that the rocksalt is dissolved by fresh water primarily along the sub-horizontal system of cracks (Fig. 5.a,b). It is also possible that the leached parts of the rocksalt were partly precipitated along the identified sealed crack network.

5.3. Salt flow dynamics in extrusive salt from identified deformation mechanisms

The movement of rocksalt from the source layer through a diapiric stem to the Earth surface is accompanied by significant changes in deformation conditions, which is accentuated by the three-dimensional nature of salt flow in the diapiric system (Talbot and Jackson, 1987). Besides decreasing temperature of deformation given by the local geotherm, the salt flow is strongly accelerated, when flowing radially from the source layer to the narrow diapiric stem and is characterized by convergent flow (Fig. 11; Talbot and Jackson, 1987; Paterson et al., 1998; Kratinová et al., 2006). The accelerating salt flow in the narrow diapiric stem is accompanied by differential stress increase. In contrast, the flow rate of salt decelerates, where the salt fountain pours out radially from its orifice on the Earth surface due to divergent flow (Talbot, 1998; Buisson and Merle, 2002, 2004; Závada et al., 2009). Microstructural evidence in this and previous studies suggests that these changes in deformation conditions throughout the entire diapiric system are recorded in the deformation microstructures. Subgrain size piezometry in our samples indicates differential stresses of 3.1–4.8 MPa, which is at least four times than we can expect in the salt glacier (less than 1 MPa in Schléder

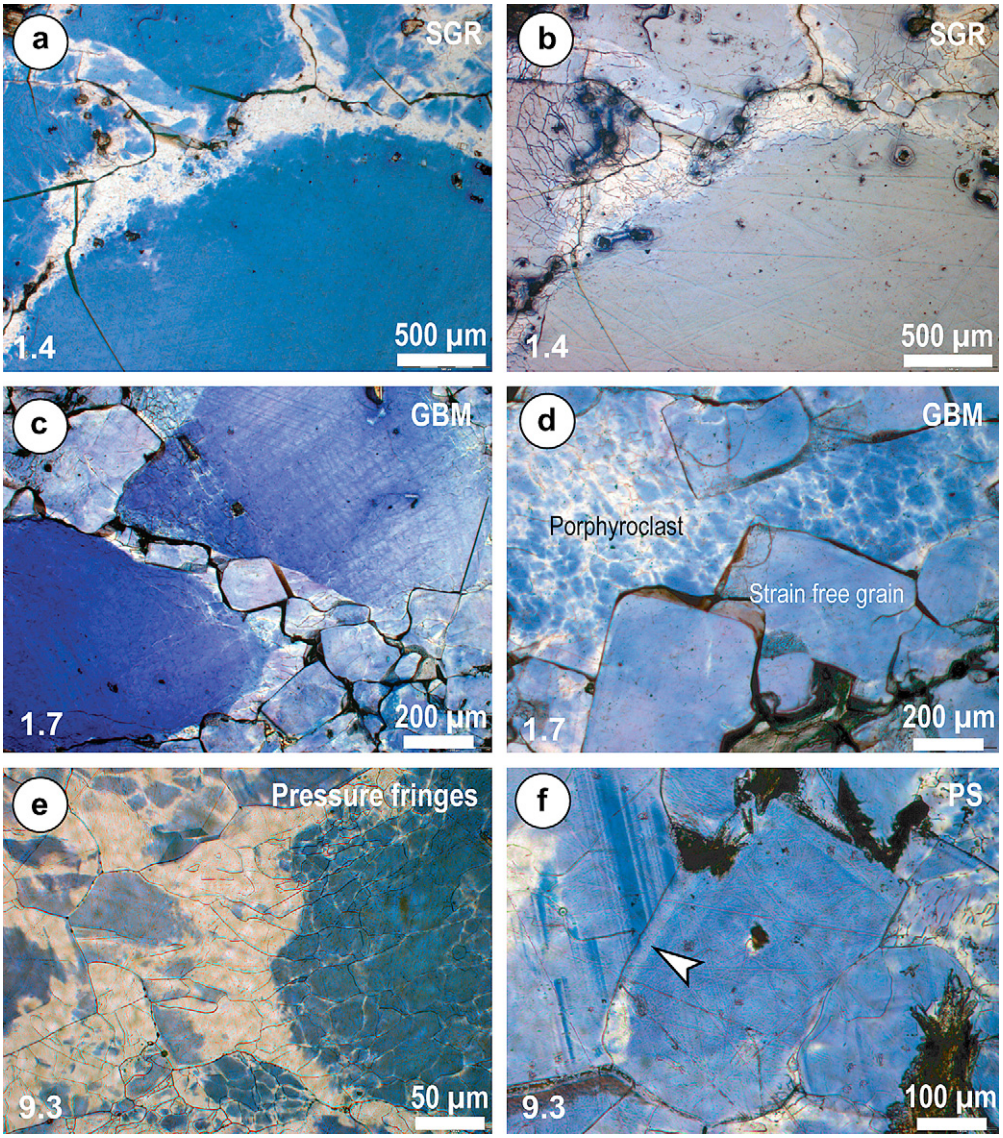

Fig. 7. Transmitted and reflected light thin section micrographs of gamma-irradiated samples collected from the front of the fountain showing details of microstructures in Fig. 7. (a) Large porphyroclasts showing deep blue core surrounded by white rim in transmitted light. (b) Same region presented in (a) but in reflected light, note that the white rim is subgrain-rich whereas the core is subgrain-free. (c) New subgrain-free grains interpreted to nucleate from subgrain-rich mantles of pophyroclasts by SGR and GBM. (d) Subgrain-free grains at subgrain-rich old grain contacts. (e) Pressure shadow behind a large subgrain-rich grain showing characteristic fringes consisting of white-pale blue elongated subgrains. (f) Small sub-euhedral grains exhibiting band microstructures are systematically truncated by indentation from the adjacent grain. On each micrograph, the stretching lineation is horizontal. Sample number is in the lower left corner of each micrograph.

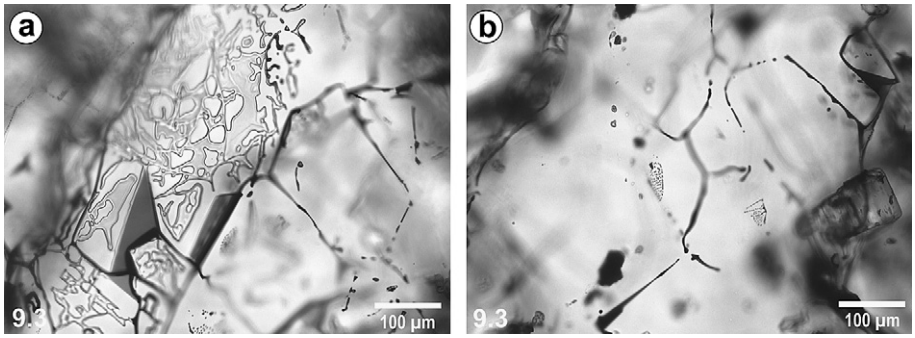

Fig. 8. Transmitted light micrographs of nongamma-irradiated sample from the front of the fountain (sample 9.3). Fluid inclusion topology on grain boundaries is typical for all samples regardless of their location. (a) Arrays of fluid inclusions at the grain boundary (upper left), micrograph shows grain boundary between porphyroclast and strain-free grain. (b) Fluid-inclusion tubes at triple point junctions between “strain-free” grains.

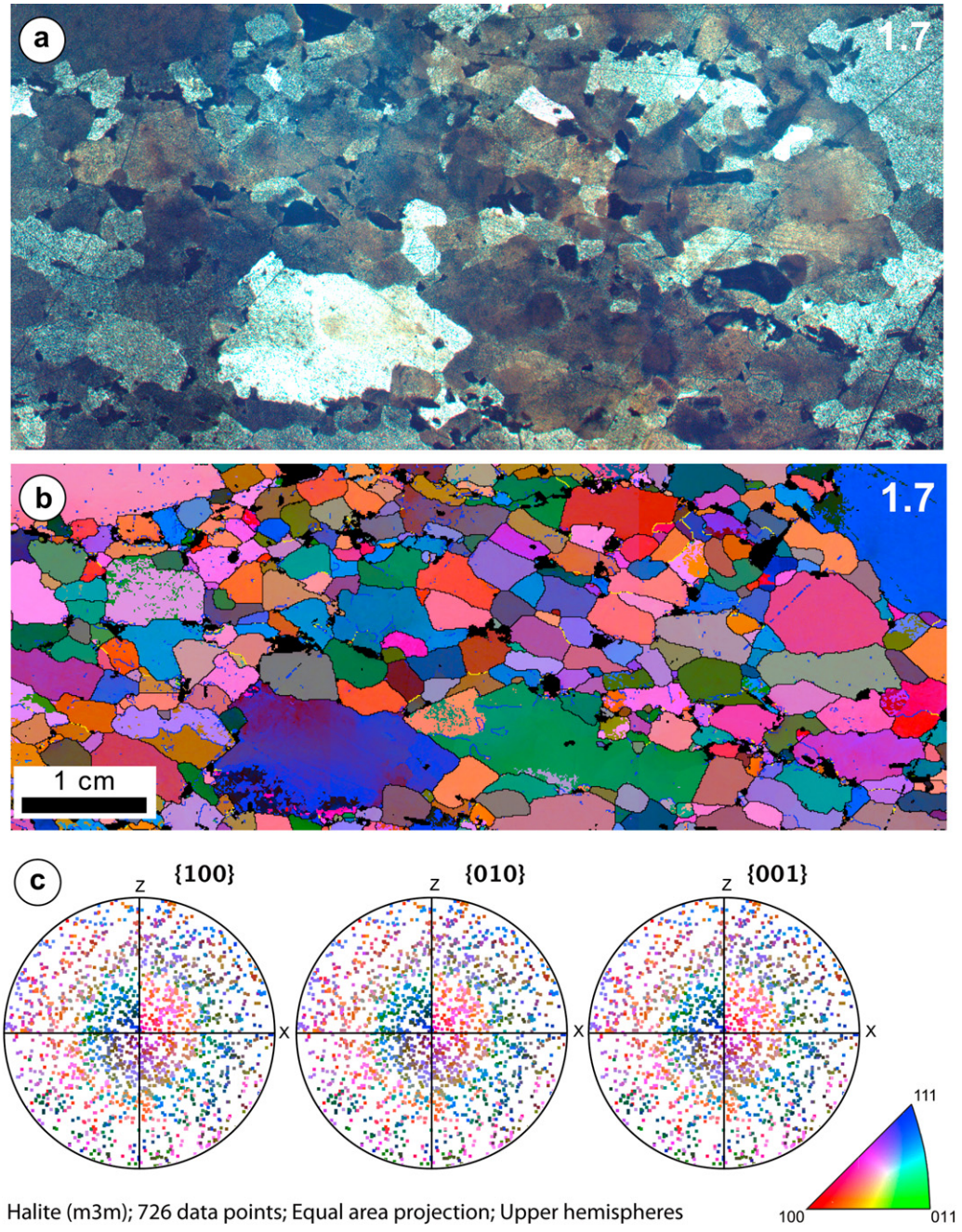

Fig. 9. EBSD measurements of the halite fabric in sample 1.7 from the distal part of the fountain. The stretching lineation is horizontal. (a) Reflected light micrograph showing area mapped by EBSD. (b) EBSD map colored according to all Euler orientations (green pixels = zero solution), created with a step size of 10 μm. Misorientation between grains was plotted using the following color code: white boundary >2–5°, blue: 5–10° misorientation, yellow: 10–15° and black: >15° misorientation. (c) Equal area, lower hemisphere projections of the crystallographic orientation data (one point per grain is plotted for total 726 grains). The dataset shows random crystallographic orientation typical for dominant PS-accommodated GBS regime.

and Urai, 2007), two times than calculated for the Garmsar hills salt glacier in central Iran (Schléder and Urai, 2007), slightly higher than the salt from diapiric wall in Klodawa salt mine (Schléder et al., 2007) and in the same range as rocksalts representing the upper part of surface-piercing diapirs by Schoenherr et al. (2009). Differential stresses calculated from piezometry are about 2× higher in the diapiric stems represented by surface piercing Ara salt in Oman than in the source layer of the same rocksalt (Schoenherr et al., 2009). Therefore, for the Qum Kuh fountain, we interpret that the subgrains in the porphyroclasts originated in the diapiric stem (Fig. 11), marked by high differential stresses during dynamic recrystallization of rocksalt governed by accelerated convergent viscous salt flow. The subgrains were then preserved within the porphyroclasts during salt flow towards the distal part of the fountain. This interpretation is in agreement with previous studies (Schléder and Urai, 2007; Schoenherr et al., 2009) and seems possible, considering that primary sedimentary features were found in porphyroclasts of surfaced rocksalt extruding from depth of 2 km (Schléder and Urai, 2007). The diapiric stem is also marked by balanced activity of SGR and GBM as also suggested for diapiric salt wall in Klodawa salt mine in Poland (Schléder et al., 2007).

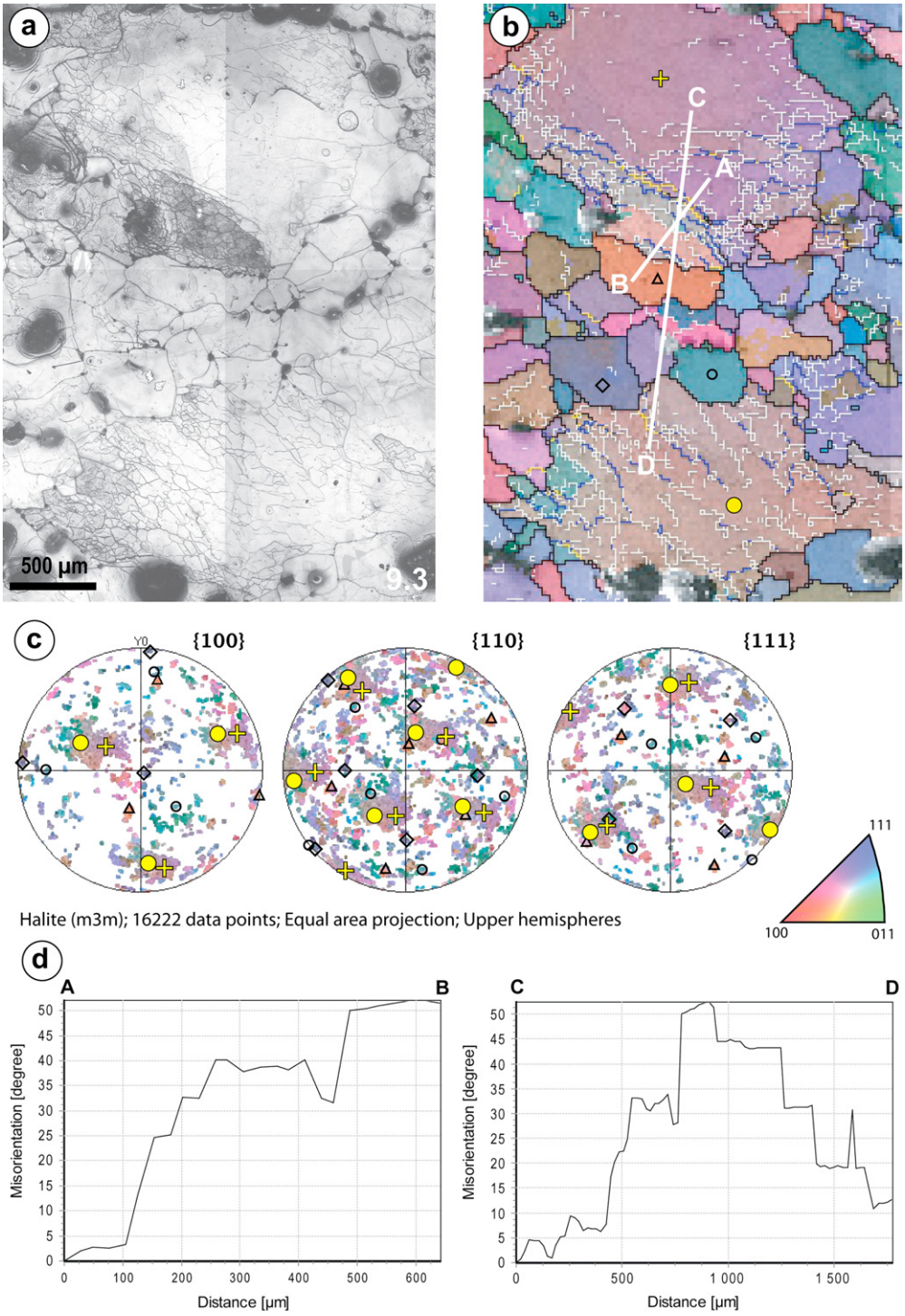

Fig. 10. EBSD measurement of an area encompassing two substructure-rich porphyroclasts (sample 9.3). (a) Reflected light micrograph showing sub-euhedral grains between the deformed grains. (b) Same area as (a), mapped with a step size of 20 µm. The map is color-coded according to all Euler orientation. White boundary: 2–5° misorientation, blue: 5–10° misorientation, yellow: 10–15° misorientation and black: >15° misorientation. Note that the upper grain has a subgrain-poor core and a subgrain-rich rim. Some subgrains at the immediate vicinity of the grain boundary reveal higher misorientation angle than the others. (c) Equal area, upper hemisphere projection of all the data points. The orientation of the substructure-rich porphyroclasts are denoted with a yellow cross and a yellow circle symbols (see image b). For comparison, orientation of three strain-free grains is also shown (see circle, diamond and triangle in image b). (d) Misorientation profiles across the EBSD map indicated in (b) reveal a systematically increasing degree of misorientation from the porphyroclast to a new adjacent grain (Profiles A-B and C-D). Profile C-D indicates step-like increase and decrease in misorientation between the two porphyroclasts in the EBSD map (b), which can represent remnants of a single large porphyroclast, considering their close crystallographic orientation (c). Starting points of these profiles (A or C) were used as reference points (i.e. 0° misorientation).

In contrast, growth of grains and subgrain boundaries growing edgewise from subgrain-rich cores (GBM, Fig. 11) reflect recovery of the aggregate during dynamic recrystallization after stress drop and salt flow deceleration, where the salt fountain pours out radially from its orifice on the Earth surface (Talbot, 1998; Buisson and Merle, 2002, 2004). Although the microstructures evince combined activity of both dynamic recrystallization (GBM) and pressure-solution-accommodated GBS, dynamic recrystallization is

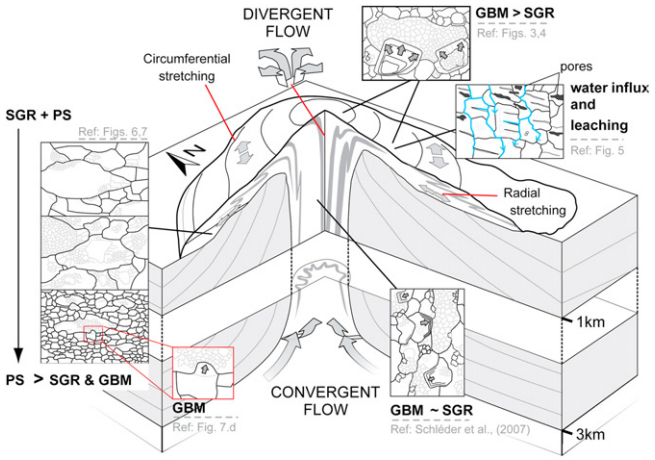

Fig. 11. Schematic diagram explaining the evolution of deformation microstructures in the entire diapiric system. The microstructural evolution reflects primarily the changing deformation conditions governed by the three-dimensional flow geometry in the diapir. From the source layer to the diapiric stem, salt flow converges radially and accelerates, which is accompanied by higher differential stresses producing small subgrains. In contrast, at the surface, salt flow diverges and therefore decelerates when flowing from the diapiric orifice. Flow kinematics of viscous extrusions (radial stretching at the base and circumferential stretching in the top part) is also depicted (Buisson and Merle, 2004; Závada et al., 2009). GBM – grain boundary migration, SGR – subgrain rotation, PS – pressure-solution creep.

clearly dominant in the top and middle part of the fountain (compare similar microstructures in Figs. 3 and 4).

Rainwater influx (Talbot and Rogers, 1980; Urai et al., 1986b; Urai and Spiers, 2007) into the salt extrusion was documented in one sample collected in the middle part of the fountain (Fig. 5). The amount of water incorporated into the salt extrusion is unknown, though it must be considerable as suggested by the semi-permanent salty lake at the southern, distal part of the fountain. However, considering the abundance of microstructures indicating pressure-solution creep in surface piercing plug of Ara salt in Oman (Schoenherr et al., 2009) in contrast to lack of such microstructures in the top of Qum Kuh fountain, we suppose that the influx of meteoric water into the fountain (Qum Kuh) was slower than into the surface piercing plug of Ara salt. This can be explained by slower viscous flow-induced extension of the surficial salt carapace and consequent extension of inter-granular channels in mature extrusions (Buisson and Merle, 2002, 2004) than in the surface piercing salt plugs or by higher precipitation rate in Oman than in central Iran.

In contrast to similar microstructures in samples from the top and middle part of the fountain, each sample from the distal part of the fountain displays different microstructures (Fig. 11). The sequence of samples 1.4, 9.3 and 1.7 is interpreted to represent a continuous microstructural evolution. While the gneiss sample 1.4 reveals core and mantle porphyroclasts and poorly developed pressure shadows with elongated subgrains, in protomylonite sample 9.3, porphyroclasts contain abundant subgrains in their entire volume and most of them are surrounded with well-developed pressure shadows with elongated subgrains (Fig. 7.e). Finally, the most intensely recrystallized sample (mylonite in this sequence) 1.7 reveals only few porphyroclasts with variable content of subgrains and large amount of subgrain-free polygonal grains. This sequence is interpreted to record an increased activity of pressure-solution (PS) creep accommodated GBS on behalf of coupled SGR and GBM accommodated dynamic recrystallization (Fig. 11).

Two interpretations can explain the textural variation of the samples 1.4, 9.3 and 1.7 from the distal part of the fountain: 1) This variation reflects a locally high strain gradient in rocksalt, which is expected at the base of the fluid extrusions (Merle, 1998; Buisson and Merle, 2004) and these samples record a continuous sequence of increasing finite strain. 2) The samples represent different original salt layers characterized by various original grain size and strength. The relatively "strong" rocksalts (represented by samples 1.4 and 9.3) deformed primarily in the diapiric stem and were then transported passively to their present position "en masse" within weaker rocksalt layers as individual porphyroclasts enclosed in the "weak" matrix of small grains in sample 1.7.

Increasing dominance of pressure-solution creep over dynamic recrystallization from the top to the distal part of the fountain is explained by influx of meteoric water into the salt fountain and also grain size decrease by combined activity of SGR and GBM. Our results are in good agreement with experimental deformation of wet fine-grained halite (Urai et al., 1986b; Peach et al., 2001; Ter Heege et al., 2005; Schléder and Urai, 2007) where solution-transfer processes dominate over crystal-plastic deformation mechanisms in fine grain halite aggregates deformed at low differential stress.

6. Conclusions

Our study of rocksalt microstructures from the Qum Kuh salt fountain confirms that gamma-irradiation is a fundamental technique for rocksalt microstructural investigations. This technique, together with EBSD analysis of crystallographic orientation and quantification of the rocksalt microstructures using the PolyLX Matlab toolbox represent a powerful approach for identification of deformation mechanisms in natural rocksalt. Concerning the study of the Qum-Kuh salt fountain, our microstructural analysis of the gamma-irradiated specimens revealed that: (1) the internal parts of porphyroclasts in all samples preserve deformation microstructures recording the high-stress deformation conditions from the diapiric stem, (2) differential stress drop and recovery of rocksalt during dynamic recrystallization and decelerating divergent flow above the extrusion orifice is reflected by grain growth and edgewise propagation of subgrains by grain-boundary migration (GBM), (3) the transition from GBM-controlled dislocation creep with subordinate solution-precipitation – grain-boundary sliding (PS-GBS) in the top and middle part of the extrusion to dominant PS-GBS with subordinate GBM and probably SGR in the distal part of the fountain, (4) the role of combined activity of GBM and SGR for grain size reduction inducing the switch from dominant dynamic recrystallization into dominant solution-precipitation creep from the top and middle part to the distal part of the fountain and (5) penetration of rainwater into the salt mass and storage of small amount of fluid in the surperficial salt mass, which is later susceptible to enhance the activity of both dynamic recrystallization and solution-precipitation accommodated GBS.

Acknowledgement

Thanks to Rolf Neuser (University of Bochum) and Jakub Haloda and Patricie Týcová (Geological Survey in Prague) for carrying out the EBSD measurements, to Jan Ter Heege (University of Bochum) for discussions on halite microstructures. C.J. Talbot and Abbas Bahroudi are acknowledged for the introduction into the geology of Qum-Kuh. People at the Geodynamic Department of Geological Survey of Iran (GSI) in Tehran are thanked for the hospitality during the 2005 field season. We are grateful to Werner Kraus, Simon Virgo, Max Arndt, Christian Diebel and Patrick Wüstefeld for the preparation of samples. Thanks also to Sandra Piazolo and Ian Alsop for their constructive reviews. This work was performed as part of UR 64/9-2, financed by the Deutsche Forschungsgemeinschaft.

References

Aftabi, P., Roustaie, M., Alsop, C.I., Talbot, C.J., 2010. InSAR mapping and modelling of an active Iranian salt extrusion. Journal of the Geological Society 167, 155–170.

Bestmann, M., Piazolo, S., Spiers, C.J., Prior, D.J., 2005. Microstructural evolution during initial stages of static recovery and recrystallization: new insights from in-situ heating experiments combined with electron backscatter diffraction analysis. Journal of Structural Geology 27 (3), 447–457.

Bestmann, M., Prior, D.J., 2003. Intragranular dynamic recrystallization in naturally deformed calcite marble: diffusion accommodated grain boundary sliding as a result of subgrain rotation recrystallization. Journal of Structural Geology 25, 1597–1613.

Bruthans, J., Filippi, M., Geršl, M., Zare, M., Melková, J., Pazdur, A., Bosák, P., 2006. Holocene marine terraces on two salt diapirs in the Persian Gulf, Iran: age, depositional history and uplift rates. Journal of Quaternary Science 21 (8), 843–857.

Buisson, C., Merle, O., 2002. Experiments on internal strain in lava dome cross sections. Bulletin of Volcanology 64 (6), 363–371.

Buisson, C., Merle, O., 2004. Numerical simulation of strain within lava domes. Journal of Structural Geology 26 (5), 847–853.

Carter, N.L., Horseman, S.T., Russel, J.E., Handin, J., 1993. Rheology of rocksalt. Journal of Structural Geology 15, 1257–1271.

Davidson, I., Bosence, D., Alsop, G.I., Al-Aawah, H., 1996. Deformation and sedimentation around active Miocene salt diapirs on the Tihama Plain, northwest Yemen. In: Alsop, G.I., Blundell, D.J., Davidson, I. (Eds.), Salt Tectonics. Special Publication No. 100, Geological Society: London, pp. 23–39.

Drury, M.R., Urai, J.L., 1990. Deformation-related recrystallization processes. Tectonophysics 172, 235–253.

Gansser, A., 1960. Die Geologische erforschung der Qum gegend, Iran. Bulletin der Vereinigung Schweizerisches Petroleum Geologen und Ingenieur 23, 1–16.

Garcia Celma, A., Donker, H. (Eds.), 1996. The Effect of Gamma Radiation in Salt EUR-Report 16743EN.

Guillopé, M., Poirier, J.P., 1980. Dynamic recrystallization during creep of single-crystalline halite: an experimental study. Journal of Geophysical Research 84, 5557–5567.

Halfpenny, A., Prior, D.J., Wheeler, J., 2004. Using electron backscattered diffraction (EBSD) to measure misorientation between 'parent' and 'daughter' grains. Implications for recrystallisation and nucleation. Materials Science Forum 467–470, 573–578.

Hudec, M.R., Jackson, M.P.A., 2007. Terra infirma: understanding salt tectonics. Earth-Science Reviews 82 (1–2), 1–28.

Jackson, M.P.A., 1985. Natural Strain in Diapiric and Glacial Rocksalt, with Emphasis on Oakwood Dome, East Texas. Bureau of Economic Geology, The University of Texas at Austin, Texas.

Jackson, M.P.A., Cornelius, R.R., Craig, C.H., Gansser, A., Stocklin, J., Talbot, C.J., 1990. Salt Diapirs of the Great Kavir, Central Iran. In: Geological Society of America, Boulder, vol. 177, 139 pp.

Jahani, S., Callot, J.P., Frizon de Lamotte, D., Letouzey, J., Leturmy, P., 2007. The Salt Diapirs of the eastern Fars province (Zagros, IRAN): a brief outline of their past and present. In: Lacombe, O., Lavé, J., Roure, F., Vergés, J. (Eds.), Thrust Belt and Foreland Basin. Springer, pp. 287–306.

Kratinová, Z., Závada, P., Hrouda, F., Schulmann, K., 2006. Non-scaled analogue modelling of AMS development during viscous flow: a simulation on diapir-like structures. Tectonophysics 418 (1–2), 51–61.

Lehner, F.K., 1995. A model for intergranular pressure solution in open systems. Tectonophysics 245 (3–4), 153–170.

Lexa, O., Štípská, P., Schulmann, K., Baratoux, L., Kröner, A., 2005. Contrasting textural record of two distinct metamorphic events of similar P–T conditions and different durations. Journal of Metamorphic Geology 23 (8), 649–666.

Li, S., Dong, M., Li, Z., Huang, S., Qing, H., Nickel, E., 2005. Gas breakthrough pressure for hydrocarbon reservoir seal rocks: implications for the security of long-term CO_2 storage in the Weyburn field. Geofluids 5, 326–334.

Littke, R., Bayer, U., Gajewski, D., Nelskamp, S. (Eds.), 2008. Dynamics of Complex Intracontinental Basins. The Central European Basin System, vol. XXIV, ISBN 978-3-540-85084-7, 520 pp. 414 illus., 358 in color. With CD-ROM., Hardcover.

McClay, K., Dooley, T., Zamora, G., 2003. Analogue models of delta systems above ductile substrates. Subsurface Sediment Mobilization, vol. 216, pp. 411–428.

Means, W.D., 1983. Microstructure and micromotion in recrystallization flow of octachloropropane, a first look. Geologische Rundschau 8, 90–98.

Means, W.D., Ree, J.H., 1988. Seven types of subgrain boundaries in octachloropropane. Journal of Structural Geology 10, 765–770.

Merle, O., 1998. Internal strain within lava flows from analogue modeling. Journal of Volcanology and Geothermal Research 81, 189–206.

Mohr, M., Warren, J.K., Kukla, P.A., Urai, J.L., Irmen, A., 2007. Subsurface seismic record of salt glaciers in an extensional intracontinental setting (Late Triassic of northwestern Germany). Geology 35, 963–966.

Muecke, N.B., 1994. Heated mud systems – a solution to squeezing-salt problems. Spe Drilling and Completion 9 (4), 276–280.

Murata, K.J., Smith, R.L., 1946. Manganese and lead coactivators of red fluorescence in halite. American Mineralogist 31, 527–538.

Passchier, C.W., Trouw, R.A.J., 2005. Microtectonics, second revised ed. Springer-Verlag Berlin and Heidelberg GmbH & Co. K, 13:978-3540640035,366 pp.

Paterson, S.R., Fowler, T.K., Schmidt, K.L., Yoshinobu, A.S., Yuan, E.S., Miller, R.B., 1998. Interpreting magmatic fabric patterns in plutons. Lithos 44, 53–82.

Peach, C., Spiers, C.J., Trimby, P.W., 2001. Effect of confining pressure on dilatation, recrystallization, and flow of rocksalt at 150 °C. Journal of Geophysical Research 106, 13315–13328.

Piazolo, S., Bestmann, M., Prior, D.J., Spiers, C.J., 2006. Temperature dependent grain boundary migration in deformed-then-annealed material: observations from experimentally deformed synthetic rocksalt. Tectonophysics 427, 55–71.

Prior, D.J., Wheeler, J., Peruzzo, L., Spiess, R., Storey, C., 2002. Some garnet microstructures: an illustration of the potential of orientation maps and misorientation analysis in microstructural studies. Journal of Structural Geology 24, 999–1011.

Ree, J.H., 1991. An experimental steady-state foliation. Journal of Structural Geology 13, 1001–1011.

Rowan, M.G., Jackson, M.P.A., Trudgill, B.D., 1999. Salt-related fault families and fault welds in the northern Gulf of Mexico. AAPG Bulletin Bulletin-American Association of Petroleum Geologists 83 (9), 1454–1484.

Salters, V.J.M., Verhoef, P.N.W., 1980. Geology and Nuclear Waste Disposal. In: Geologica Ultraiectina Special Publication, vol. 1. Instituut voor Aardwetenschappen der Rijksuniversiteit te Utrecht, Institute of Earth Sciences, Utrecht, 399 pp.

Schenk, O., Urai, J.L., 2005. The migration of fluid-filled grain boundaries in recrystallizing synthetic bischofite: first results of in-situ high-pressure, high-temperature deformation experiments in transmitted light. Journal of Metamorphic Geology 23, 695–709.

Schenk, O., Urai, J.L., 2004. Microstructural evolution and grain boundary structure during static recrystallization in synthetic polycrystals of sodium chloride containing saturated brine. Contributions to Mineralogy and Petrology 146, 671–682.

Schléder, Z., 2006. Deformation mechanisms of naturally deformed rocksalt. PhD thesis from RWTH Aachen University, 162 pp.

Schléder, Z., Urai, J.L., 2005. Microstructural evolution of deformation-modified primary halite from the Middle Triassic Röt Formation at Hengelo, The Netherlands. International Journal of Earth Sciences 94, 941–955.

Schléder, Z., Urai, J.L., 2007. Deformation and recrystallization mechanisms in mylonitic shear zones in naturally deformed extrusive Eocene-Oligocene rocksalt from Eyvanekey plateau and Garmsar hills (central Iran). Journal of Structural Geology 29, 241–255.

Schléder, Z., Burliga, S., Urai, J.L., 2007. Dynamic and static recrystallization-related microstructures in halite samples from the Klodawa salt wall (central Poland) as revealed by gamma-irradiation. Neues Jahrbuch Fur Mineralogie-Abhandlungen 184, 17–28.

Schoenherr, J., Schléder, Z., Urai, J.L., Fokker, P.A., Schulze, O., 2007a. Deformation mechanisms and rheology of Pre-cambrian rocksalt from the south Oman Salt Basin. In: Wallner, Lux, Minkley, Hardy Jr., (Eds.), The Mechanical Behavior of Salt – Understanding of THMC Processes in Salt. Taylor & Francis Group, London, ISBN 978-0-415-44398-2, pp. 167–173.

Schoenherr, J., Schléder, Z., Urai, J.L., Littke, R., Kukla, P.A., 2009. Deformation mechanisms of deeply buried and surface-piercing Late Pre-Cambrian to Early Cambrian Ara Salt from interior Oman. International Journal of Earth Sciences 3 (8), 167–173. doi:10.1007/s00531-009-0443-3.

Schoenherr, J., Urai, J.L., Kukla, P.A., Littke, R., Schléder, Z., Larroque, J.M., Newall, M. J., Al-Abry, N., Al-Siyabi, H.A., Rawahi, Z., 2007b. Limits to the sealing capacity of rocksalt: a case study of the Infra-cambrian Ara salt from the south Oman Salt Basin. AAPG Bulletin 91 (11), 1541–1557. doi:10.1306/06200706122.

Schmatz, J., Urai, J.L., 2009. The interaction of fluid inclusions and migrating grain boundaries in transmitted light experiments of recrystallising rock analogue camphor. Journal of Metamorphic Geology 28 (1), 1–18.

Schutjens, P.M.T.M., Spiers, C.J., 1999. Intergranular pressure solution in NaCl: grain-to-grain experiments under the optical microscope. Oil and Gas Science and Technology 54, 729–750.

Spiers, C.J., Carter, N.L., 1998. Microphysics of rocksalt flow in nature. In: Aubertin, M., Hardy, H.R. (Eds.), The Mechanical Behaviour of Salt. Proceedings of the Fourth Conference Series on Rock and Soil Mechanics, vol. 22. TTP Trans Tech Publications, Clausthal-Zellerfeld, pp. 115–128.

Spiers, C.J., De Meer, S., Niemeijer, A.R., Zhang, X., 2004. Kinetics of rock deformation by pressure solution and the role of thin aqueous films. In: Nakashima, S. (Ed.), Physico-chemistry of Water in Geological and Biological Systems. Universal Academy Press, Inc., pp. 129–158.

Spiers, C.J., Schutjens, P.M.T.M., Brzesowsky, R.H., Peach, C.J., Liezenberg, J.L., Zwart, H.J., 1990. Experimental determination of constitutive parameters governing creep of rocksalt by pressure solution. In: Knipe, R.J., Rutter, E.H. (Eds.), Deformation Mechanisms, Rheology and Tectonics. Special Publication-Geological Society of London, vol. 54, pp. 215–227.

Stipp, M., Stuenitz, H., Heilbronner, R., Schmid, S.M., 2002. Dynamic recrystallization of quartz: correlation between natural and experimental conditions. In: De Meer, S., de Bresser, J.H.P., Pennock, G.M. (Eds.), Deformation Mechanisms, Rheology and Tectonics: Current Status and Future Perspectives. Geological Society of London, Special Publications, vol. 200, pp. 171–190.

Talbot, C.J., 1998. Extrusions of Hormuz salt in Iran, Lyell. The Past Is The Key To The Present, vol. 143, pp. 315–334.

Talbot, C.J., Aftabi, P., 2004. Geology and models of salt exreusion at Qum Kuh, central Iran. Journal of the Geological Society 161, 321–334.

Talbot, C.J., Alavi, M., 1996. The past of the future syntaxis across the Zagros. In: Alsop, G., Blundell, D., Davison, I. (Eds.), Salt Tectonics. Geological Society Special Publication, vol. 100, pp. 89–109.

Talbot, C.J., Jackson, M.P.A., 1987. Internal kinematics of salt diapirs. AAPG Bulletin 71 (9), 1068–1093.
Talbot, C.J., Rogers, E., 1980. Seasonal movements in an Iranian salt glacier. Science 208, 395–397.
Ter Heege, J.H., De Bresser, J.H.P., Spiers, C.J., 2005. Rheological behaviour of synthetic rocksalt: the interplay between water, dynamic recrystallization and deformation mechanisms. Journal of Structural Geology 27, 948–963.
Trimby, P.W., Drury, M.R., Spiers, C.J., 2000. Misorientations across etched boundaries in deformed rocksalt: a study using electron backscatter diffraction. Journal of Structural Geology 22, 81–89.
Urai, J.L., 1983. Water assisted dynamic recrystallization and weakening in polycrystalline bischofite. Tectonophysics 96 (1–2), 125–157.
Urai, J.L., 1987. Development of microstructure during deformation of carnallite and bischofite in transmitted light. In: Zwart, H.J., Martens, M., van der Molen, I., Passchier, C.W., Spiers, C., Vissers, R.L.M. (Eds.), Tectonic and Structural Processes on a Macro-, Meso- and Micro-scale. Tectonophysics, vol. 135, pp. 251–263.
Urai, J.L., Spiers, C.J., Zwart, H.J., Lister, G.S., 1986a. Dynamic recrystallisation of minerals. In: Hobbs, B.E., Heard, H.C. (Eds.), Mineral and Rock Deformation; Laboratory Studies; the Paterson Volume. AGU Geophysical Monograph 36. American Geophysical Union, Washington, DC, USA, pp. 161–199.
Urai, J.L., Spiers, C.J., Zwart, H.J., Lister, G.S., 1986b. Weakening of rocksalt by water during long term creep. Nature 324, 554–557.
Urai, J.L., Schléder, Z., Spiers, C.J., Kukla, P.A., 2008. Flow and transport properties of salt rocks. In: Littke, R., Bayer, U., Gajewski, D., Brink, H.J., Winter, I. (Eds.), Dynamics of Complex Intracontinental Basins: The Central European Basin System, pp. 2–5.
Urai, J.L., Spiers, C.J., 2007. The effect of grain boundary water on deformation mechanisms and rheology of rocksalt during long-term deformation. In: Wallner, M., Lux, K., Minkley, W., Hardy Jr., H. (Eds.), The Mechanical Behavior of Salt – Understanding of THMC Processes in Salt, Hannover, Germany, pp. 149–158.
Urai, J.L., Spiers, C.J., Peach, C., Franssen, R.C.M.W., Liezenberg, J.L., 1987. Deformation mechanisms operating in naturally deformed halite rocks as deduced from microstructural investigations. Geologie en Mijnbouw 66, 165–176.
Van Opbroek, G., den Hartog, H.W., 1985. Radiation damage of NaCl: dose rate effects. Journal of Physics C: Solid State Physics 18, 257–268.
Watanabe, T., Peach, C.J., 2002. Electrical impedance measurement of plastically deforming halite rocks at 125 °C and 50 MPa. Journal of Geophysical Research 107 ECV 2-1–ECV 2-12.
Weinberger, R., Lyakhovsky, V., Baer, G., Begin, Z.B., 2006. Mechanical modeling and InSAR measurements of Mount Sedom uplift, Dead Sea basin: implications for effective viscosity of rocksalt. Geochemistry Geophysics Geosystems 7 (5). doi:10.1029/2005GC001185.
Wilson, S., Fossum, A., Fredrich, J., 2002. Assessment of salt loading on well casings. IADC/SPE Drilling Conference.
Závada, P., Kratinová, Z., Kusbach, V., Schulmann, K., 2009. Internal fabric development in complex lava domes. Tectonophysics 466 (1–2), 101–113.